Check for updates

Near-infrared probe-based confocal microendoscope for deep-tissue imaging

JIAFU WANG,[1,2] HUA LI,[1,2] GENG TIAN,[1,2] YONG DENG,[1,2] QIAN LIU,[1,2] AND LING FU[1,2,*]

[1]*Britton Chance Center for Biomedical Photonics, Wuhan National Laboratory for Optoelectronics, Huazhong University of Science and Technology, Wuhan, Hubei 430074, China*
[2]*MoE Key Laboratory for Biomedical Photonics, Collaborative Innovation Center for Biomedical Engineering, School of Engineering Sciences, Huazhong University of Science and Technology, Wuhan, Hubei 430074, China*
[*]lfu@mail.hust.edu.cn

Abstract: In this work, a near-infrared probe-based confocal microendoscope (pCM) with a 785 nm laser source, a long working distance, and a probe with diameter of 2.6 mm that can be compatible with a conventional endoscope is demonstrated to produce deep-tissue images at cellular resolutions with enhanced contrast and signal-to-noise ratio. Theoretical simulations and experiments confirm that near-infrared light can optimize the image quality. Abundant details of mouse esophagus obtained at different depths demonstrate the system's ability to image deep tissues at cellular resolutions, which makes it possible to diagnose diseases in the digestive tract in real time, laying a solid foundation for clinical applications.

1. Introduction

The confocal microendoscope (CM) is a diagnostic device that is fundamentally technically different from other endoscopes, and can observe histological details during an ongoing endoscopy, at cellular resolutions [1,2]. Conventional CMs combine a 488 nm laser source, a pinhole to geometrically eliminate out-of-focus light, and an agent of fluorescein sodium for tissue labelling [1,3]. Optical biopsy, which is the process of visualizing epithelial cells in real time using a CM, has been applied in the diagnosis of Barrett's esophagus [4], gastritis [5], colorectal cancer [6], lung cancer [7], cervical diseases [8], ovarian diseases [9], and other digestive [10] and respiratory diseases [7]. However, it is difficult to observe the structures under lamina propria using confocal microendoscopy at 488 nm, because of the intense scattering of visible light [11,12]. For instance, muscularis mucosae at depths of more than 250 μm are useful for the classification of tumor invasion [13] and further treatment [12], but they need new technologies and instruments to be visualized.

Near-infrared light permits deep-tissue imaging with reduced scattering and low autofluorescence [14,15], and is applied in optical coherence tomography (OCT) [16,17], two-photon fluorescence (TPF) [18], and second harmonic generation (SHG) imaging [19]. In addition, the light absorption by hemoglobin and water, the major optical absorbers in human tissues, is much lower in the spectrum range from 650 nm to 900 nm than at shorter wavelengths [20]. Furthermore, the excitation wavelength of indocyanine green (ICG), the only near-infrared agent that has been clinically validated, is approximately 785 nm, which also falls in the wavelength range mentioned above [21]. Consequently, the near-infrared spectrum window is suitable for diagnosis and therapy [22].

A dual-axis CM [23,24] suitable for colonoscopies and confocal laparoscopies [11] on liver was designed with near-infrared excitation light. However, as the miniature scanners were integrated at the distal ends of the optical fiber probes, the diameter of the scanhead or the rigid probe was more than 5 mm, which was not suitable for conventional gastrointestinal endoscopes. In comparison, a probe-based CM (pCM) had a proximal scanning mechanism

and a miniature objective, giving rise to a flexible probe that could go through the biopsy channel of a digestive endoscope [25,26]. A pCM with the excitation wavelength of 785 nm and imaging depth of 40 μm was developed to characterize liver nodules [25].

Aiming to achieve deep-tissue imaging at cellular resolutions using gastrointestinal endoscopes, we present a demonstration of a near-infrared pCM with a long working distance of 300 μm and a 2.6 mm diameter optical fiber probe that can be inserted through the biopsy channel of a gastrointestinal endoscope. A miniature objective is the key to meet the requirements of long working distance, high resolution, and wide field of view (FOV). Although near-infrared light increases the radius of the Airy disk in the image space more than visible light does, the miniature objective can still be implemented by using near-infrared light. Muscularis mucosae of the esophagus, at a depth of approximately 250 μm, which could not be imaged using the visible microendoscopes, could now be observed using the near-infrared microendoscope system based on a home-made near-infrared miniature objective. The normal tissues in colon and abnormal tissues of ulcerative colitis showed obvious feature differences at different depths up to 300 μm, demonstrating the clinical potential of the proposed near-infrared pCM.

2. Monte Carlo simulation of light transport in tissues

In the human body, light is scattered by cells and fibers and absorbed by chromophores such as hemoglobin after entering the tissues [27]. In order to choose a suitable wavelength for deep-tissue imaging, it is necessary to understand the light transport in tissues at different wavelengths and estimate the penetration depths [28]. In our work, light transport in mouse colon was investigated by performing Monte Carlo simulations at three wavelengths: 488 nm, 785 nm, and 1064 nm, which were chosen to cover both the visible and near-infrared regions. Absorption distributions of the beams focused into turbid media were modelled [29,30]. The focal lengths of the beams were 2100 μm with a numerical aperture of 0.92 in water. The long focal lengths of 2100 μm can reflect the absorption distributions of different wavelengths. The focal lengths were far greater than the depths of the focal points. Here, the depth of the focal point is the distance from the focal point to the interface in the distribution of the absorption density [30].

The absorption coefficient μ_a and scattering coefficient μ_s of mouse colon were measured in the wavelength range from 450 nm to 1100 nm using a spectrophotometer (Lambda 950, PerkinElmer). Before measurements, the processes of obtaining colon tissues are the same to routine experiments. The measurements consist of thickness measurements, transmission measurements and reflection measurements. Based on the thickness, transmittance, and reflectance of each specimen, the absorption coefficient μ_a and reduced scattering coefficient μ_s' were calculated by using the inverse adding-doubling method [31]. The refractive index n and anisotropy factor g of mouse colon were derived from references [32,33]. According to the reduced scattering coefficient μ_s' and anisotropy factor g, scattering coefficient μ_s was calculated by $\mu_s = \mu_s' / (1-g)$. As the fluorescence imaging corresponds to agent, healthy mice weighed approximately 20 g were administrated ICG by intravenous injection with dosages of 5 mg/kg, 10 mg/kg, 15 mg/kg, 20 mg/kg, and 25 mg/kg. There were 11 mice for each dosage and 11 healthy mice for stroke-physiological saline solution with equal volume to ICG solution. All the parameters were measured in the same setup. The measurement results show that the absorption coefficient and scattering coefficient of colon tissues with no agents are similar to those of colon tissues with agents, demonstrating that the influence of ICG solution on absorption coefficient and scattering coefficient of mouse colon can be neglected. Finally, the average values were obtained. All the coefficients

are shown in Table 1. The measured absorption coefficient and scattering coefficient decrease with the increase in the wavelength.

Table 1. Optical parameters of mouse colon

λ (nm)	n	μ_a (cm^{-1})	μ_s (cm^{-1})	g
488	1.35	0.92	108.43	0.88
785	1.34	0.74	50.50	0.91
1064	1.33	0.46	42.07	0.92

Figure 1 shows the two-dimensional distributions of the absorption density based on parameters in Table 1, i.e., the absorption probability density of the incident photons per unit volume, in the turbid colon of a mouse, obtained through Monte Carlo simulations. The depths of the focal points for 488 nm, 785 nm, and 1064 nm are 467 μm, 1149 μm, and 1391 μm, respectively, characterizing the penetration depths of the incident photons. Near-infrared light can penetrate deeper than blue light in a tissue. In the cases of 785 nm and 1064 nm, the penetration depth is enhanced at longer wavelengths, but the depth increment is gentle, approximately 240 μm. Therefore, light of 785 nm and 1064 nm can result in relatively close penetration depths. This might be due to the smooth variation of the absorption and scattering coefficients between 750 nm and 1000 nm. The excitation spectrum of ICG has a peak at 785 nm and a full width at half maximum of approximately 55 nm. By considering both the penetration depth of the illumination light and the excitation efficiency of ICG, 785 nm appears to be an optimal excitation wavelength for near-infrared confocal imaging in clinical applications.
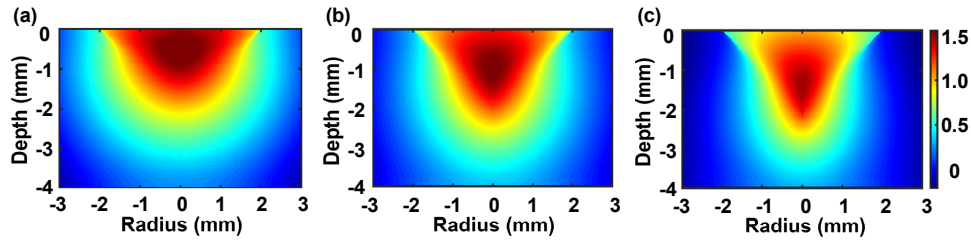

Fig. 1. Distributions of the absorption density of illumination light at (a) 488 nm, (b) 785 nm, and (c) 1064 nm in mouse colon.

3. Near-infrared miniature objective

The miniature objective focuses the laser from the optical fiber bundle onto the tissue and collects the fluorescence back into the optical fiber bundle. The difficulty in its design and manufacturing is mainly because of its small diameter and high numerical aperture [34]. In order to image muscularis mucosae with working wavelengths between 780 nm and 860 nm, and be compatible with biopsy channel, a near-infrared miniature objective with a long working distance of 300 μm, an adequate magnification of 2 ×, a diameter of 2.6 mm, and a length less than 10 mm is indispensable. In addition, to achieve diffraction-limited performance, the root mean square (RMS) spot size in fiber bundle space should be less than the diffraction-limited Airy disk spot size [34]. Firstly, the magnification M of the near-infrared miniature objective can be calculated by the following formula:

$$M = \frac{NA_{obj}}{NA_{ima}}, \tag{1}$$

where NA_{obj} is the NA in the object space and NA_{ima} is the NA in the image space. Secondly, the Airy disk radius r_{Airy} in the image space can be described as follows:

$$r_{Airy} = \frac{0.61\lambda}{NA_{ima}}, \tag{2}$$

where λ is the wavelength. Finally, according to the two equations above, the relationship between the Airy disk radius and magnification can be expressed by the following equation:

$$r_{Airy} = \frac{0.61\lambda}{NA_{obj}} M. \tag{3}$$

Since the radius of the Airy disk is proportional to wavelength, the Airy disk at near-infrared wavelengths is larger than that at visible wavelengths. For a 785 nm laser, the radius of the Airy disk should be approximately 2.00 μm, considering the NA matching between the near-infrared miniature objective and an optical fiber that has an NA of approximately 0.3 [35]. Since ICG is used as the fluorescence indicator, the working wavelength of the miniature objective is between 780 and 860 nm. Taking all these factors into consideration, one effective way is to reduce the RMS radius of the spot diagram to ensure higher light intensity is transmitted through an individual fiber in the optical fiber bundle. As the radius of each fiber in the optical fiber bundle is approximately 1.50 μm, the RMS radius should be less than this radius. In order to realize the reduction in RMS radius, a glass (H-ZLAF92) with higher refractive index, which can cause greater refraction for the beam, was used for the first lens of the miniature objective. In addition, a plastic (PMMA), which is easier to be manufactured, instead of glass was used for the 5th lens, comparing with the miniature objective that used for visible light. Thus, a structure with five lenses, as shown in Fig. 2, is confirmed as the final configuration of the optical layout of the near-infrared miniature objective. In addition, the seawater with a refractive index similar to tissue was assumed for the 300 μm gap between the front edge of the first lens and the tissue. The correction of chromatic aberration is realized primarily by the inclusion and optimization of the second and third lenses. The fourth lens is used to correct the spherical aberration and the last lens is used to correct residual aberrations. As the main aberrations were corrected and the length of the miniature objective should be less than 10 mm, there was no need to add additional lenses to correct minor aberrations.
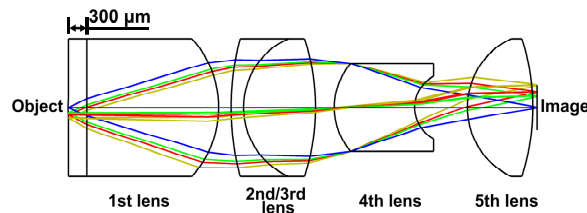

Fig. 2. Schematic diagram of the near-infrared miniature objective.

As shown in Fig. 2, the working distance of miniature objective is 300 μm. The NA_{obj} and NA_{ima} were 0.48 and 0.24, respectively, meeting the 2 × magnification requirements. Additionally, the 0.24 NA_{ima} can approximately match the 0.3 NA of fiber in the optical fiber bundle.

Spot diagrams of the optical system were optimized for 785 nm, 820 nm, and 860 nm, and are shown in Fig. 3. The near-infrared miniature objective was designed with a full field of 360 μm. In the 0.000 mm field, the low aberration barely affects the imaging quality. Some coma was present in the 0.180 mm and 0.250 mm fields and some astigmatism was present in the 0.360 mm field, which increased the RMS radius. This maximum RMS radius was less than 2.00 μm, the radius of the diffraction-limited Airy disk, indicating diffraction-limited performance for the near-infrared miniature objective. The maximum RMS radius of 1.284

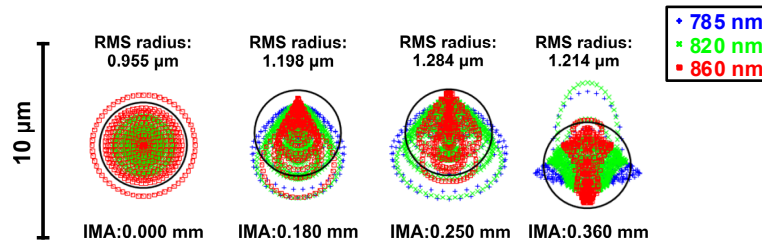μm was also less than 1.50 μm, the radius of the individual fibers in the optical fiber bundle, which met the design requirements.

Fig. 3. Spot diagrams of four radial image positions: 0.000 mm, 0.180 mm, 0.250 mm, and 0.360 mm. Airy disk radius is 1.930 μm.

Figure 4 represents the modulation transfer function (MTF) curves in the tangential plane and sagittal plane for the four fields. The Nyquist spatial cutoff frequency is the reciprocal of two sampling intervals. As the fibers in the bundle are in a quasi-hexagonal arrangement, the sampling interval depends on the arrangement of the fibers and distance d between the neighboring fiber cores. For all the sampling intervals, Nyquist spatial cut-off frequency is f corresponding to maximal sampling interval. In this quasi-hexagonal arrangement, maximal sampling interval is $\sqrt{3}d\,/\,2$. So the Nyquist spatial cut-off frequency f can be calculated using the following equation [36,37]:

$$f = \frac{1}{\sqrt{3}d}. \tag{4}$$

From Eq. (4), the cut-off frequency of the near-infrared miniature objective will be 186 lp/mm as d is 3.10 μm. The moduli of the optical transfer function (OTF) are higher than 0.45 at the cut-off frequency and the MTF curves are near diffraction-limited, indicating the high contrast of the near-infrared miniature objective.
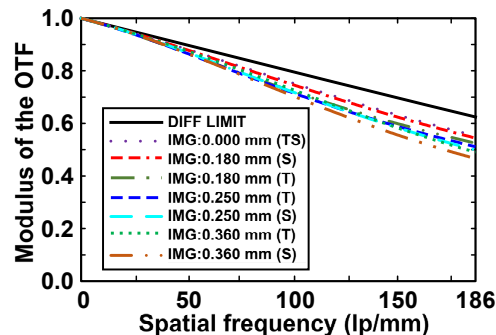

Fig. 4. Polychromatic diffraction MTFs of the near-infrared miniature objective. DIFF LIMIT: diffraction limit, T: tangential plane, S: sagittal plane.

Based on the above design, five lenses were manufactured and assembled into a near-infrared miniature objective with a working distance of 300 μm, diameter of 2.6 mm, and length of 8.5 mm. The near-infrared miniature objective and one of the lenses are shown in Fig. 5. The lateral resolution of the near-infrared miniature objective was tested by using a standard 1951 US Air Force (USAF) target. The smallest resolvable features were the group 9 element 3 bars, which corresponded to a resolution of 0.775 μm, meeting the requirements of cellular imaging.
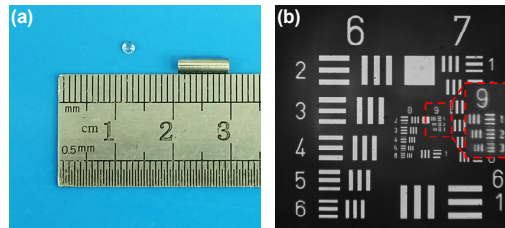
Fig. 5. Near-infrared miniature objective and its resolution measurement. (a) Near-infrared miniature objective and one of the lenses in it. (b) Resolution measurement of near-infrared miniature objective.

4. Near-infrared pCM setup and sample preparation

4.1 Near-infrared pCM setup

An effective approach to obtain images with high contrast is to acquire a confocal system. The schematic of this near-infrared pCM system is similar to that of our previous system that is a visible pCM [26,34]. Excitation light generated by a 785 nm laser (OBIS 785 LX, Coherent) was expanded by a beam expander and reflected by a dichroic mirror (DM, Di02-R785-25 × 36, Semrock). Subsequently, a two-dimensional scanning system, which consisted of an X-scanner (CRS, Cambridge) and a Y-scanner (6215H, Cambridge) scanned the beam in the two-dimensional plane. After the scanning, the beam was relayed into the back aperture of the objective lens (UMPLANFL N 20 × /0.50, Olympus), which coupled the excitation light into the proximal end of the optical fiber bundle in the probe. Finally, the beam was focused onto the sample by a near-infrared miniature objective, which also collected the emitted fluorescence from the sample. The fluorescence at longer wavelengths were transmitted along the same path and passed through the dichroic mirror and a bandpass filter (FF01-835/70-25, Semrock). After passing the bandpass filter, the fluorescence was focused by a lens to pass through a pinhole that was placed at the focus of the condenser. The pinhole was used to reject the out-of-focus light. Finally, a photomultiplier tube (PMT, R3896, Hamamatsu) was used to acquire the optical signals and convert them into electrical signals.

With the X-Y scanners, the imaging speed can reach 5 fps, which makes imaging in real time possible. Each frame consists of 1024 × 1024 pixels, so each pixel dwell time is approximately 0.19 μs.

Before the experiments, a newly made optical fiber probe, which consisted of an optical fiber bundle and a near-infrared miniature objective with a diameter of 2.6 mm and length of 8.5 mm, was passed through the biopsy channel in a clinical endoscope, as shown in Fig. 6. The optical fiber probe could also be used independently in a mouse for *in vivo* tissue imaging in real time without a conventional endoscope (Fig. 6(e)).
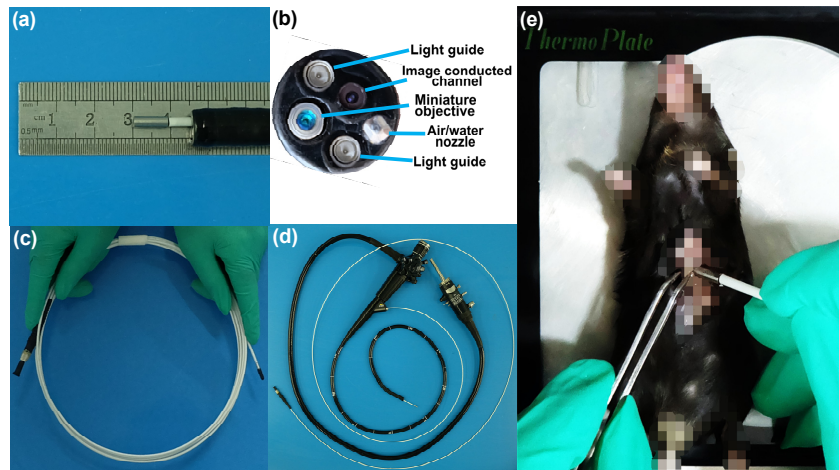
Fig. 6. Optical fiber probe and imaging of mouse *in vivo*. (a) Probe goes through the biopsy channel in conventional endoscope. (b) End face of probe in conventional endoscope. (c) Optical fiber probe with a near-infrared miniature objective. (d) Optical fiber probe is compatible with conventional endoscope. (e) Photograph of optical fiber probe placed into the stomach of a mouse.

4.2 Sample preparation

We tested the performance of the system by imaging the liver and tissues in the digestive tract of C57BL/6 mice. The mice were purchased from the Zhongnan Hospital of Wuhan University (Wuhan, China), and weighed approximately 20 g before our experiments. The mice were maintained under specific-pathogen-free conditions with controlled temperature and humidity, from the beginning to the end, and were adapted to the relevant surroundings with free access to normal food and water for at least two weeks before the experiments. All mice were healthy before the experiments. For tissue imaging in the digestive tract, in order to reduce the impact of food residue, the mice were fasted for 24 h before the experiments with continuous access to water. All experiments were approved by the animal experiment guidelines of the Animal Experimentation Ethics Committee of the Huazhong University of Science and Technology (HUST, Wuhan, China).

The dextran sulphate sodium (DSS)-induced ulcerative colitis model is one of the widely used models for biological research [38,39]. 5% (w/v) DSS was administered orally in the drinking water of the C57BL/6 mice for seven days. The control group drank normal water, as usual. Both the experimental group and control group were used for deep-tissue imaging.

In order to improve the contrasts of the images, fluorescein sodium and ICG were used in the 488 nm visible pCM system and 785 nm near-infrared pCM system, respectively. Both agents are permitted in clinical applications by intravenous injection. Laser powers were typically 0.5 to 1.5 mW at the surface of the tissues. 20 mg/kg and 80 mg/kg injections of fluorescein sodium were administered intravenously for imaging the liver and tissues in gastrointestinal tract, respectively, in the 488 nm visible pCM system. 0.3 mg/kg and 15 mg/kg injections of ICG were administered intravenously for imaging the liver and gastrointestinal tract, respectively, in the 785 nm near-infrared pCM system. After intravenous injection, fluorescein sodium was found to bind extensively to the serum albumin [40] and ICG was found to bind intensely to the plasma proteins, albumin or alpha-lipoprotein [11,41]. Before imaging, the mice were anaesthetized by intraperitoneal injection of urethane and chloral-hydrate mixed solution (90 μL/10 g) and then administrated fluorescein sodium or ICG. The tissues were marked within 30 s after administrating and images were obtained in real time. Before imaging, the stroke-physiological saline solution was dripped on the tissues.

As the esophagus is near the heart, the heart beating is detrimental to image. So we obtained the images of esophagus *ex vivo* and other tissues *in vivo*.

5. Imaging characterization of near-infrared pCM

5.1 Lateral resolution

The lateral resolution of the system is a crucial parameter that determines whether the system can observe cells in tissues or not. According to the Rayleigh criterion [42], a longer wavelength is usually detrimental to the lateral resolution. However, for a system based on the optical fiber bundle, the lateral resolution depends on the distance between the neighboring fiber cores, instead of on the wavelength [43]. A fiber core with a center-to-center spacing of 3.10 μm will be unable to identify cells [34]. With the help of a near-infrared miniature objective, however, an increased resolution will be possible, as shown in Fig. 7(a), which shows the imaging of a standard 1951 USAF target with a drop of ICG solution. In Fig. 7(b), the smallest resolvable features are the group 8 element 3 bars in the red oval, corresponding to a resolution of 1.55 μm, which is high enough to observe the cells in the tissues. The lateral resolution of the system is limited by the interspaces of neighboring fibers, not by the diffraction of the miniature objective.

5.2 FOV

Initially, the FOV of the near-infrared pCM was determined by the active area of the optical fiber bundle. With the addition of the near-infrared miniature objective to the fiber tip, the actual FOV becomes half of the active area of the fiber due to the objective magnification of 2. As the magnification was 2 × , the actual FOV would become half of the diameter of the optical fiber bundle. In order to test the effective FOV of the system, a grating (80 lines/mm, Edmund) was put in contact with the distal end of the probe. As shown in Fig. 7(c), 26.5 stripes of the grating could be distinguished clearly with an FOV of 330 μm, which represents a wide observation area.
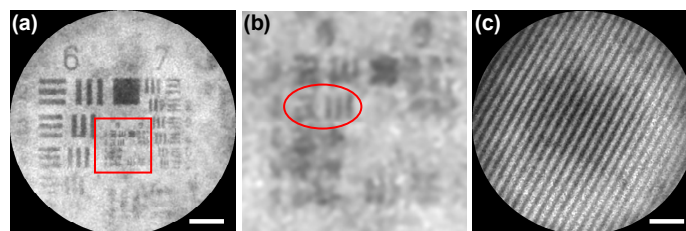

Fig. 7. Lateral resolution and FOV measurement. (a) Image of the USAF target. (b) Enlarged details of the red rectangle in (a). (c) Image of the grating.

5.3 Contrast

The contrast of the system is another crucial parameter that determines its ability to distinguish details. For tissue imaging, by taking advantage of the stronger penetration ability and slower depth-dependent attenuation of near-infrared light, the image contrast can be enhanced to more than that of visible-light pCM. As a result, the detector can collect more signals and the SNR will be improved.

To test the contrast of our system, *in vivo* images of the surfaces of colon mucosae were obtained with visible pCM and near-infrared pCM, as shown in Fig. 8(a) and Fig. 8(b), respectively. The images of visible pCM and near-infrared pCM were acquired using systems with 488 nm and 785 nm lasers, respectively. Columnar epithelial cells could be observed in both the figures. The contrast of the images acquired by near-infrared pCM was higher than that of the images acquired by visible pCM.
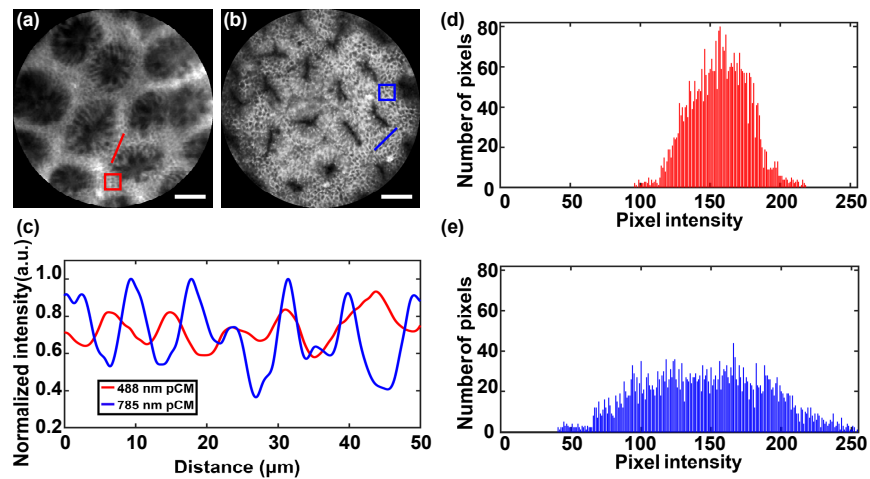
Fig. 8. Image contrast measurement of colon by visible pCM and near-infrared pCM. (a,b) Images of colon by visible pCM and near-infrared pCM. (c) Normalized intensity values along the lines in (a) and (b). (d, e) Histograms of gray values in the rectangles of (a) and (b). Scale bars: 50 μm.

In order to quantify the effect on image quality enhancement, the normalized intensities along the red and blue straight lines labelled in Fig. 8(a) and Fig. 8(b) were analyzed, as shown in Fig. 8(c). The obvious ups and downs in the intensities of the signals acquired by the near-infrared pCM with dyeing agent of ICG show a contrast higher than that of visible pCM with dyeing agent of fluorescein sodium. Histogram analysis, performed by choosing an area of an image and counting the gray values in it, can be used to describe the gray information of the images. As the agents of the visible pCM and near-infrared pCM were different and the images of the same region in tissue could not be obtained by the handheld probes of the two systems, each area we chose in the image should be a region where the cells were clear. As shown in Fig. 8(a) and Fig. 8(b), red and blue rectangular areas were chosen and the corresponding histograms are shown in Fig. 8(d) and Fig. 8(e), respectively. An image with the histogram of gray values concentrated at the middle will be a low-contrast image. Here, the near-infrared pCM with dyeing agent of ICG exhibits a significantly wider spread of pixel intensities, compared to the visible pCM with dyeing agent of fluorescein sodium, indicating a higher contrast. For the imaging contrast, in addition to wavelength, the dyeing agent of ICG may also contribute to high contrast. In a word, the contrasts of images obtained by near-infrared pCM with dyeing agent of ICG are higher than the contrasts of images obtained by visible pCM with dyeing agent of fluorescein sodium.

In addition to the colon, some other tissues were also imaged by the visible pCM and near-infrared pCM, as shown in Fig. 9. In the esophagus, squamous epithelium could be observed in Fig. 9(a), Fig. 9(d) and Fig. 9(g). The images obtained by visible pCM and near-infrared pCM, while sharing many similarities, provide different information in some respects. The most obvious difference is that the images acquired by near-infrared pCM show higher SNR and contrast than those acquired by visible pCM. For example, in the stomach, the gastric pits could be seen for both wavelengths; however, the images acquired by the near-infrared pCM were clear enough to identify almost every columnar epithelial cell, whereas, this identification was difficult in the case of visible pCM, as shown in Fig. 9(b) and Fig. 9(e). Figure 9(h) shows the stomach structures in the histologic specimen. In the liver, hepatocytes that contacted with one another were distributed regularly into hepatic cords, as shown in Fig. 9(f). These cords, which were too bright and lacked contrast, were separated by neighboring vascular sinusoids, as shown in Fig. 9(c) and Fig. 9(f). Figure 9(i) shows the liver structures in the histologic specimen. The images of the various tissues showed obvious SNR and

contrast improvements for the near-infrared pCM, enabling image acquisition of tissues with more details or higher quality.
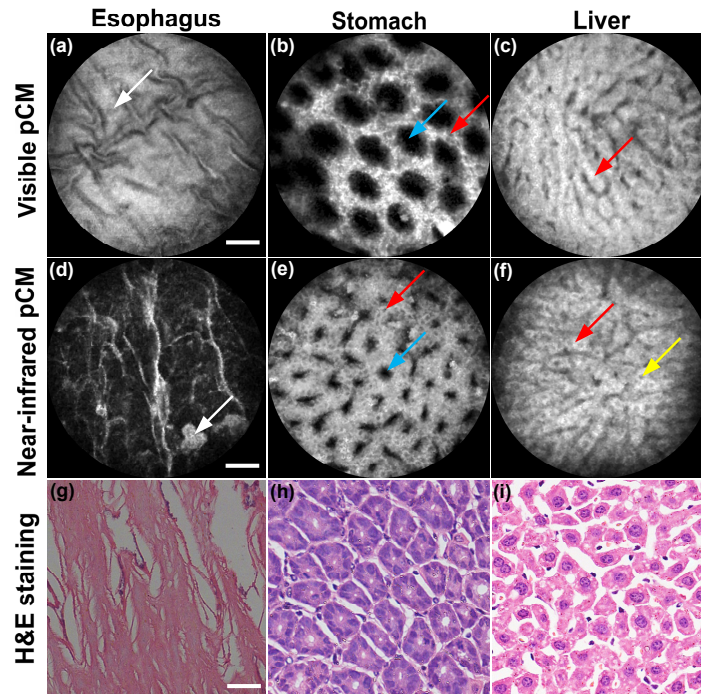

Fig. 9. Images of various tissues by visible pCM and near-infrared pCM. (a-c) and (d-f) show the images obtained by 488 nm excitation and 785 nm excitation, respectively. (a) and (d) are images of the esophagus. White arrows show the squamous epithelium. (b) and (e) are images of the stomach. Red arrows indicate superficial epithelial cells and blue arrows indicate gastric pits. (c) and (f) show images of the liver. Red arrows indicate the sinusoidal architecture of the liver and yellow arrow indicates the nucleus of the hepatocyte. (g-i) Corresponding histologic specimens. Scale bars: 50 μm.

6. Deep tissue imaging

6.1 Deep imaging of esophagus

To validate our system's ability for muscularis mucosae imaging, experiments on excised mouse esophagus were carried out using visible pCM and near-infrared pCM. Before experiments, the probe with fixed working distance of 300 μm was fixed on the translation stage (562-XYZ, Newport). As the esophagus was prepared, the micrometer with precision of 0.5 μm was rotated manually and the probe moved toward the esophagus. Since the surface of the esophagus could be observed, we began to record the imaging and the position of micrometer. During the whole process, the probe was almost in contact with the tissues and did not compress the tissues. So all the parameters maintained the same at each depth. Tissue images of different depths were obtained, as shown in Fig. 10.
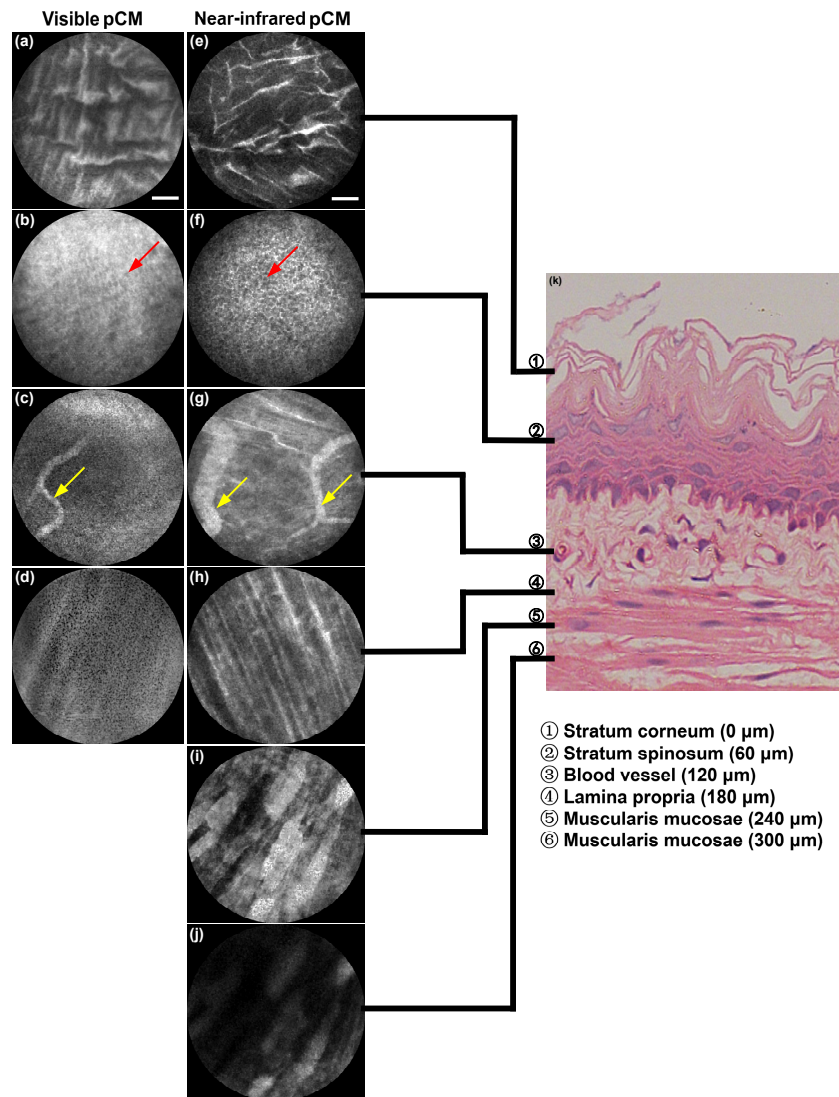
Fig. 10. Deep tissue images of mouse esophagus by visible pCM and near-infrared pCM. (a-d) Images were obtained by 488 nm excitation. (e-j) Images were obtained by 785 nm excitation. (k) H&E staining. Red arrows: cells in stratum spinosum layer, yellow arrows: blood vessels. Scale bars: 50 μm.

Figure 10(a-d) show the squamous epithelium in the stratum corneum, dense cells in the stratum spinosum, vessels in the third layer, and fine fibers in the lamina propria of the esophagus, respectively, obtained by visible pCM. From the comparisons with the images obtained by near-infrared pCM, shown in Fig. 10(e-h), it can be observed that same structure exhibits higher SNR and contrast for near-infrared pCM. Figure 10(h-j) show that the images obtained by the near-infrared system are clear enough to observe both the fine clear fibers in the lamina propria and the coarse orderly fibers in the muscularis mucosae, which are buried in the local background in visible pCM images. All these images at different depths show obvious stratification, which is consistent with the histologic esophagus, as shown in Fig. 10(k). These results at different depths of esophagus demonstrate that near-infrared pCM can achieve deeper tissue images with higher SNR and contrast than visible pCM, which provides a new method to observe structures in different layers of tissues.

6.2 Deep imaging of ulcerative colitis

To demonstrate the capability of near-infrared pCM for disease diagnosis in deep-layer tissues, the colon of one mouse with ulcerative colitis was imaged, and compared with that of a mouse in the control group, without ulcerative colitis. The imaging process was the same to that of the deep imaging of esophagus. Different depths of normal colon tissues and tissues with ulcerative colitis are shown in Fig. 11.
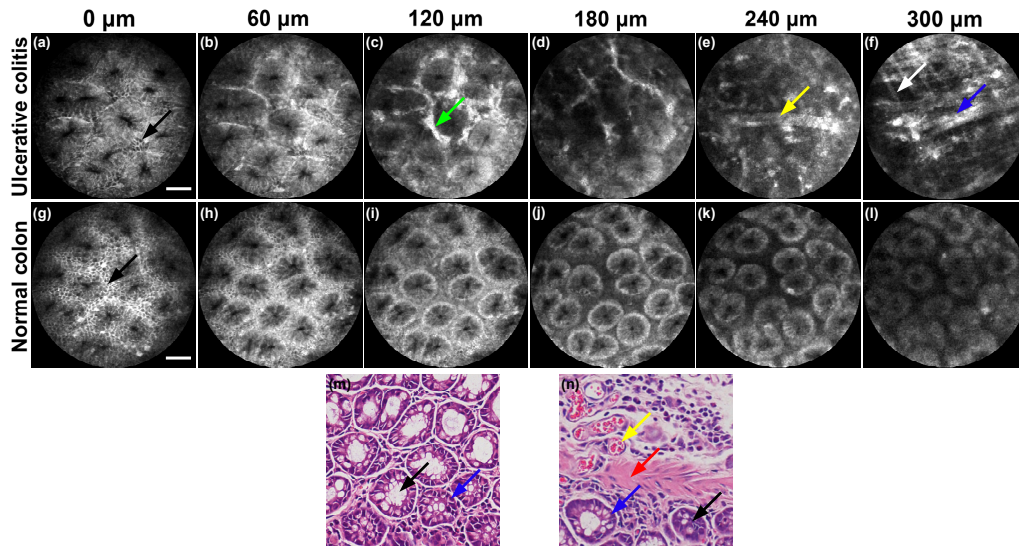

Fig. 11. Different depth images of tissues of normal colon and colon with ulcerative colitis. (a-f) Different depth images of ulcerative colitis. (g-l) Different depths images of normal tissues of colon. (a) and (g) Columnar epithelial cells (black arrows) and crypts can be seen on the surface of both tissues. (c) Ulcerative colitis shows ICG leakage (green arrow) between crypts. (d) Ulcerative colitis shows irregular crypts with ICG leakage. (e) Blood vessel (yellow arrow) can be seen without crypt structures. (f) Fibers with strong fluorescence in layer of muscularis mucosae can be seen in ulcerative colitis (white arrow and blue arrow). (g-l) Signal intensity falls and there is hardly a change in the structure with increasing imaging penetration depth. (m) and (n) correspond to histologic specimens of normal and ulcerative colitis tissues. In (m) and (n), black arrows: crypts; blue arrows: columnar epithelial cells; yellow arrow: blood vessel; red arrow: fiber in muscularis mucosae. Scale bars: 50 μm.

In the case of ulcerative colitis, the colon surface is similar to that of a normal colon. Columnar epithelial cells are clearly arranged in an orderly manner in a radial mode, surrounding the crypts, as shown in Fig. 11(a) and 11(g). However, goblet cells are missing and the columnar epithelial cells are decreasing. At a depth of 60 μm, as shown in Fig. 11(b) and 11(h), a colon with ulcerative colitis and normal tissues share many similarities, while leakage of ICG appears in the colon with ulcerative colitis. With a further increase in the depth, severe leakage of ICG results in intense fluorescence in the extravascular space, which cannot be observed in normal colon tissues, as shown in Fig. 11(c) and 11(i). Moreover, the tissues with ulcerative colitis are characterized by the leakage of ICG into the extravascular space with almost no crypts, at a depth of 180 μm, and show significant differences from normal tissues in colon at the same depth, as shown in Fig. 11(d) and 11(j).

At the depth of 240 μm, a blood vessel labelled with ICG with intense fluorescence can be observed in the colon with ulcerative colitis with no crypts, which cannot be observed in the normal tissues, as shown in Fig. 11(e) and 11(k). As the crypts can only be seen on the surface of the tissue and in the lamina propria, the different structures at this depth indicate that the lamina propria of ulcerative colitis is thinner than that of normal colon tissues. Owing to the deep imaging depth of the near-infrared pCM, the blood vessel can be observed and

captured. This blood vessel is at a deep layer of tissue, which will not be observed if the working distance of the probe is less than this depth.

As shown in Fig. 11(f), at 300 μm, which is the deepest the light of the probe can reach, both fine and thick fibers can be observed in different directions at the layer of muscularis mucosae in ulcerative colitis. Moreover, the fibers at this layer are intensively dyed because they are rich in plasma proteins, which is highly different from fibers at the same depth of normal colon tissues. In normal tissues with no ulcerative colitis, no structures can be seen in the muscularis mucosae, indicating that the muscularis mucosae in normal tissues is at a depth deeper than 300 μm. Since the working distance of our probe is 300 μm, the structures of muscularis mucosae in deeper layers in ulcerative colitis can be obtained, corresponding to histologic specimens, as shown in Fig. 11(m) and 11(n). However, these structures will not be observed by other microendoscopes with limited working distances.

7. Conclusion and discussion

In this study, we developed a near-infrared pCM for deep tissues, with a wide FOV. To the best of our knowledge, this is the first time a study has demonstrated that the near-infrared pCM can image at a depth of 300 μm with cellular resolution in digestive tract with a probe diameter of only 2.6 mm. A near-infrared miniature objective corrected various aberrations to meet the requirements of long working distance and high cellular resolution. Deep tissue imaging was achieved based on theoretical analysis and experimental verification, using near-infrared light. The performance of the near-infrared pCM was measured, confirming that a cellular visualization with a wide FOV could be realized. With these characteristics, our near-infrared pCM was used for imaging the digestive tract and liver of a mouse. The images of the different layers of the esophagus showed the system's ability to image the muscularis mucosae. Furthermore, the images of a mouse with ulcerative colitis at different depths showed structures distinct from normal colon tissues, confirming that the near-infrared pCM was able to diagnose diseases at a greater penetration depth in the gastrointestinal tract, than visible pCM.

A further research will focus on dual focal imaging that can visualize the surface and the depth simultaneously to obtain more structure information for diagnosis. Moreover, as this near-infrared pCM system is used for imaging on mice, a new near-infrared pCM system that can be used for humans is on the agenda. In order to design the new near-infrared pCM system, Monte Carlo simulations will simulate on human tissues. As digestive tract includes epithelium, lamina propria and muscularis mucosae in mucosa, and submucosa, the 300 μm working distance can observe the lamina propria in large and small intestine of human [1,44,45]. For the cancer invasion with depths more than 300 μm, or even 500 μm, microendoscopes with longer working distance will be helpful. In the future, after entering the clinical applications, the probe of near-infrared pCM can be used as an accessory device of conventional endoscopy to diagnose diseases such as intestinal metaplasia and cancer in digestive tract with high efficiency with no need for subsequent examinations. The near-infrared pCM can be used for deep tissue imaging to inspect early lesions in mucosa.

facility support. The authors also thank the Animal Experimentation Ethics Committee of HUST.

Disclosures

The authors declare that there are no conflicts of interest related to this article.

References and links

1. R. Kiesslich, J. Burg, M. Vieth, J. Gnaendiger, M. Enders, P. Delaney, A. Polglase, W. McLaren, D. Janell, S. Thomas, B. Nafe, P. R. Galle, and M. F. Neurath, "Confocal laser endoscopy for diagnosing intraepithelial neoplasias and colorectal cancer *in vivo*," Gastroenterology **127**(3), 706–713 (2004).
2. E. Laemmel, M. Genet, G. Le Goualher, A. Perchant, J. F. Le Gargasson, and E. Vicaut, "Fibered confocal fluorescence microscopy (Cell-viZio) facilitates extended imaging in the field of microcirculation. A comparison with intravital microscopy," J. Vasc. Res. **41**(5), 400–411 (2004).
3. J. M. Jabbour, M. A. Saldua, J. N. Bixler, and K. C. Maitland, "Confocal endomicroscopy: instrumentation and medical applications," Ann. Biomed. Eng. **40**(2), 378–397 (2012).
4. T. Shah, R. Lippman, D. Kohli, P. Mutha, S. Solomon, and A. Zfass, "Accuracy of probe-based confocal laser endomicroscopy (pCLE) compared to random biopsies during endoscopic surveillance of Barrett's esophagus," Endosc. Int. Open **6**(4), E414–E420 (2018).
5. T. Liu, H. Zheng, W. Gong, C. Chen, and B. Jiang, "The accuracy of confocal laser endomicroscopy, narrow band imaging, and chromoendoscopy for the detection of atrophic gastritis," J. Clin. Gastroenterol. **49**(5), 379–386 (2015).
6. T. Hlavaty, M. Huorka, T. Koller, P. Zita, E. Kresanova, B. Rychly, and J. Toth, "Colorectal cancer screening in patients with ulcerative and Crohn's colitis with use of colonoscopy, chromoendoscopy and confocal endomicroscopy," Eur. J. Gastroenterol. Hepatol. **23**(8), 680–689 (2011).
7. F. S. Fuchs, S. Zirlik, K. Hildner, J. Schubert, M. Vieth, and M. F. Neurath, "Confocal laser endomicroscopy for diagnosing lung cancer *in vivo*," Eur. Respir. J. **41**(6), 1401–1408 (2013).
8. C. Schlosser, N. Bodenschatz, S. Lam, M. Lee, J. N. McAlpine, D. M. Miller, D. J. T. Van Niekerk, M. Follen, M. Guillaud, C. E. MacAulay, and P. M. Lane, "Fluorescence confocal endomicroscopy of the cervix: pilot study on the potential and limitations for clinical implementation," J. Biomed. Opt. **21**(12), 126011 (2016).
9. M. D. Risi, A. R. Rouse, S. K. Chambers, K. D. Hatch, W. Zheng, and A. F. Gmitro, "Pilot clinical evaluation of a confocal microlaparoscope for ovarian cancer detection," Int. J. Gynecol. Cancer **26**(2), 248–254 (2016).
10. Y. Nakai, H. Isayama, S. Shinoura, T. Iwashita, J. B. Samarasena, K. J. Chang, and K. Koike, "Confocal laser endomicroscopy in gastrointestinal and pancreatobiliary diseases," Dig. Endosc. **26**(1), 86–94 (2014).
11. M. Goetz, I. Deris, M. Vieth, E. Murr, A. Hoffman, P. Delaney, P. R. Galle, M. F. Neurath, and R. Kiesslich, "Near-infrared confocal imaging during mini-laparoscopy: a novel rigid endomicroscope with increased imaging plane depth," J. Hepatol. **53**(1), 84–90 (2010).
12. O. Pech, T. Rabenstein, H. Manner, M. C. Petrone, J. Pohl, M. Vieth, M. Stolte, and C. Ell, "Confocal laser endomicroscopy for *in vivo* diagnosis of early squamous cell carcinoma in the esophagus," Clin. Gastroenterol. Hepatol. **6**(1), 89–94 (2008).
13. C. Katada, M. Muto, K. Momma, M. Arima, H. Tajiri, C. Kanamaru, H. Ooyanagi, H. Endo, T. Michida, N. Hasuike, I. Oda, T. Fujii, and D. Saito, "Clinical outcome after endoscopic mucosal resection for esophageal squamous cell carcinoma invading the muscularis mucosae--a multicenter retrospective cohort study," Endoscopy **39**(9), 779–783 (2007).
14. J. V. Frangioni, "*In vivo* near-infrared fluorescence imaging," Curr. Opin. Chem. Biol. **7**(5), 626–634 (2003).
15. K. Seker and M. Engin, "Deep tissue near-infrared imaging for vascular network analysis," J. Innov. Opt. Health Sci. **10**(3), 1650051 (2017).
16. H. Makhlouf, A. R. Rouse, and A. F. Gmitro, "Dual modality fluorescence confocal and spectral-domain optical coherence tomography microendoscope," Biomed. Opt. Express **2**(3), 634–644 (2011).
17. A. F. Fercher, W. Drexler, C. K. Hitzenberger, and T. Lasser, "Optical coherence tomography - principles and applications," Rep. Prog. Phys. **66**(2), 239–303 (2003).
18. E. E. Hoover and J. A. Squier, "Advances in multiphoton microscopy technology," Nat. Photonics **7**(2), 93–101 (2013).
19. T. A. Theodossiou, C. Thrasivoulou, C. Ekwobi, and D. L. Becker, "Second harmonic generation confocal microscopy of collagen type I from rat tendon cryosections," Biophys. J. **91**(12), 4665–4677 (2006).
20. M. Miwa and T. Shikayama, "ICG fluorescence imaging and its medical applications," Proc. SPIE **7160**, 373–378 (2008).
21. N. Haj-Hosseini, P. Behm, I. Shabo, and K. Wardell, "Fluorescence spectroscopy using indocyanine green for lymph node mapping," Proc. SPIE **8935**, 1–6 (2014).
22. L. Shi, L. A. Sordillo, A. Rodríguez-Contreras, and R. Alfano, "Transmission in near-infrared optical windows for deep brain imaging," J. Biophotonics **9**(1-2), 38–43 (2016).
23. G. Li, H. Li, X. Duan, Q. Zhou, J. Zhou, K. R. Oldham, and T. D. Wang, "Visualizing epithelial expression in vertical and horizontal planes with dual axes confocal endomicroscope using compact distal scanner," IEEE Trans. Med. Imaging **36**(7), 1482–1490 (2017).

24. W. Piyawattanametha, H. Ra, Z. Qiu, S. Friedland, J. T. C. Liu, K. Loewke, G. S. Kino, O. Solgaard, T. D. Wang, M. J. Mandella, and C. H. Contag, "*In vivo* near-infrared dual-axis confocal microendoscopy in the human lower gastrointestinal tract," J. Biomed. Opt. **17**(2), 021102 (2012).
25. A. Pierangelo, D. Fuks, P. Validire, A. Benali, and B. Gayet, "Diagnostic accuracy of confocal laser endomicroscopy for the characterization of liver nodules," Eur. J. Gastroenterol. Hepatol. **29**(1), 42–47 (2017).
26. J. F. Wang, M. Yang, L. Yang, Y. Zhang, J. Yuan, Q. Liu, X. H. Hou, and L. Fu, "A confocal endoscope for cellular imaging," Engineering **1**(3), 351–360 (2015).
27. T. Maeda, N. Arakawa, M. Takahashi, and Y. Aizu, "Monte Carlo simulation of spectral reflectance using a multilayered skin tissue model," Opt. Rev. **17**(3), 223–229 (2010).
28. L. Wang, S. L. Jacques, and L. Zheng, "MCML--Monte Carlo modeling of light transport in multi-layered tissues," Comput. Methods Programs Biomed. **47**(2), 131–146 (1995).
29. L. Wang and S. L. Jacques, "Monte Carlo Modeling of light transport in multi-layered tissues in standard C," University of Texas M. D. Anderson Cancer Center (1992).
30. L. V. Wang and G. Liang, "Absorption distribution of an optical beam focused into a turbid medium," Appl. Opt. **38**(22), 4951–4958 (1999).
31. S. A. Prahl, M. J. C. van Gemert, and A. J. Welch, "Determining the optical properties of turbid mediaby using the adding-doubling method," Appl. Opt. **32**(4), 559–568 (1993).
32. P. Giannios, S. Koutsoumpos, K. G. Toutouzas, M. Matiatou, G. C. Zografos, and K. Moutzouris, "Complex refractive index of normal and malignant human colorectal tissue in the visible and near-infrared," J. Biophotonics **10**(2), 303–310 (2017).
33. A. N. Bashkatov, E. A. Genina, V. I. Kochubey, V. S. Rubtsov, E. A. Kolesnikova, and V. V. Tuchin, "Optical properties of human colon tissues in the 350 – 2500 nm spectral range," Quantum Electron. **44**(8), 779–784 (2014).
34. L. Yang, J. Wang, G. Tian, J. Yuan, Q. Liu, and L. Fu, "Five-lens, easy-to-implement miniature objective for a fluorescence confocal microendoscope," Opt. Express **24**(1), 473–484 (2016).
35. Y. S. Sabharwal, A. R. Rouse, L. Donaldson, M. F. Hopkins, and A. F. Gmitro, "Slit-scanning confocal microendoscope for high-resolution *in vivo* imaging," Appl. Opt. **38**(34), 7133–7144 (1999).
36. R. Drougard, "Optical Transfer Properties of Fiber Bundles," J. Opt. Soc. Am. **54**(7), 907–914 (1964).
37. J. Lv, B. Xue, T. Li, Y.-h. He, X.-l. Ma, and X.-t. Yan, "Optical system design of subminiature endoscope with imaging fiber bundle," Proc. SPIE **10153** 101530L (2016).
38. D. N. Seril, J. Liao, G. Y. Yang, and C. S. Yang, "Oxidative stress and ulcerative colitis-associated carcinogenesis: studies in humans and animal models," Carcinogenesis **24**(3), 353–362 (2003).
39. L. A. Dieleman, M. J. Palmen, H. Akol, E. Bloemena, A. S. Peña, S. G. M. Meuwissen, and E. P. Van Rees, "Chronic experimental colitis induced by dextran sulphate sodium (DSS) is characterized by Th1 and Th2 cytokines," Clin. Exp. Immunol. **114**(3), 385–391 (1998).
40. A. L. Polglase, W. J. McLaren, S. A. Skinner, R. Kiesslich, M. F. Neurath, and P. M. Delaney, "A fluorescence confocal endomicroscope for *in vivo* microscopy of the upper- and the lower-GI tract," Gastrointest. Endosc. **62**(5), 686–695 (2005).
41. S. Yoneya, T. Saito, Y. Komatsu, I. Koyama, K. Takahashi, and J. Duvoll-Young, "Binding properties of indocyanine green in human blood," Invest. Ophthalmol. Vis. Sci. **39**(7), 1286–1290 (1998).
42. J. B. Pawley, in *Handbook of Biological Confocal Microscopy* (Springer, 2008), Chap. 10.
43. H. Zhang, J. Yuan, and L. Fu, "Imaging Fourier transform endospectroscopy for *in vivo* and *in situ* multispectral imaging," Opt. Express **20**(21), 23349–23360 (2012).
44. S. Carvalho, N. Gueiral, E. Nogueira, R. Henrique, L. Oliveira, and V. Tuchin, "Wavelength dependence of the refractive index of human colorectal tissues: comparison between healthy mucosa and cancer," J. Biomed. Photon. Eng. **2**(4), 040307 (2016).
45. J. S. Trier and T. H. Browning, "Morphologic response of the mucosa of human small intestine to x-ray exposure," J. Clin. Invest. **45**(2), 194–204 (1966).